RSC Advances

PAPER

View Article Online
View Journal | View Issue

Cite this: *RSC Adv.*, 2020, **10**, 22080

Electrodeposited nickel–graphene nanocomposite coating: effect of graphene nanoplatelet size on its microstructure and hardness

Tran Van Hau,[ac] Pham Van Trinh,[*a] Nguyen Phuong Hoai Nam,[c] Nguyen Van Tu,[a] Vu Dinh Lam,[b] Doan Dinh Phuong,[ab] Phan Ngoc Minh[b] and Bui Hung Thang*[ab]

Received 27th April 2020
Accepted 4th June 2020

DOI: 10.1039/d0ra03776a

rsc.li/rsc-advances

In this study, the effect of graphene nanoplatelet (GNP) size on the microstructure and hardness of the electrodeposited nickel–graphene nanocomposite coatings were investigated. GNPs with different sizes were prepared by using a high energy ball milling technique. The experimental result revealed the high energy ball milling technique could reduce the size, increase the surface area, and improve the dispersion ability of GNPs. The microstructure, hardness, and components of the nanocomposite coatings were greatly affected by GNP sizes. The highest microhardness was measured to be 273 HV for the nanocomposite coatings containing 5 h-milled GNPs, which is increased up to ~47% compared to pristine Ni coating. The enhancement in the hardness is attributed to the uniform dispersion of the small GNP sizes inside the Ni matrix and the Ni grain size reduction when using milled GNPs.

1. Introduction

Electrodeposition is a popular technique for preparing metal and alloy coatings such as nickel (Ni), chrome (Cr), zinc (Zn), copper (Cu), nickel–cobalt (Ni–Co), nickel–zinc (Ni–Zn), copper–zinc (Cu–Zn), *etc.* on the surface of conductive materials.[1–7] In this technique, Ni is widely used to fabricate the coating for protecting the surface of metals from wear and corrosion. Recently, it was found that the mechanical properties of the Ni coating can be significantly improved by adding silicon carbide (SiC), aluminum oxide (Al_2O_3), titanium dioxide (TiO_2) nanoparticles, carbon nanotubes (CNTs) and graphene (Gr) as the reinforcement materials to the Ni matrix.[8–10] Among them, graphene has emerged as a promising reinforcement material because it possesses extraordinary mechanical properties such as sustaining breaking strengths of 42 N m^{-1}, an intrinsic mechanical strain of ~25% and Young's modulus of 1.0 TPa, tensile strength of 130 GPa, and a surface area of 2.63×10^7 cm^2 g^{-1}.[11–14] In addition, Gr is an impermeable material with chemical stability. Therefore, Gr is used for composites, energy storage applications, semiconductors, heat spreaders,[15–21] *etc.* Some recent studies demonstrated the important role of Gr in the metal composite field such as enhancing thermal conductivity, electrical conductivity, the synergistic strengthening.[12,22] Many studies have shown that the Gr reinforced Ni coating (Ni/Gr) and graphene oxide (GO) reinforced Ni coating (Ni/GO) exhibited an enhancement in the microhardness, anticorrosion, wear resistance, the tribological properties than those of pure Ni coating.[23–28] Some attempts have conducted to investigate the influence of temperature, the pulse-reverse electrodeposition technique concerning the mechanical properties of Gr reinforced Ni coating.[29–31] Y. Liu *et al.* have controlled the microstructure and mechanical properties of electrodeposited Ni/Gr composite. The result showed that the tensile strength of Ni/Gr composite coating was 864 MPa and a plastic elongation of 20.6%.[32] Some studies of G. Yashin *et al.* investigated in detail the effects including the surfactant concentration, deposition current density on the morphology and mechanical properties of Ni/Gr composite coating. All of those results showed the significant microhardness improvement of Ni/Gr composite coating.[33–36]

In the composite field, the properties of reinforcement material play an important role in the strengthening effects. Some studies have demonstrated the influence of Gr aspect ratio on the microstructure and mechanical properties of the Gr/metal composite and Gr/polymer composites. In 2014, G. Dai *et al.* reported the influence of the aspect ratio, shape, clustering, orientation and volume fraction of graphene platelets on the mechanical behavior and damage mechanisms of nanocomposites by 3D computational model of graphene reinforced polymer composites.[37] In 2015, F. Wang *et al.* demonstrated that graphene nanoplatelets (GNPs)/epoxy composites had higher modulus and strength with increasing concentration of small GNP sizes.[38] In addition, the effect of the aspect ratio of GNPs on

[a]*Institute of Materials Science, Vietnam Academy of Science and Technology, 18 Hoang Quoc Viet Str., Cau Giay Distr., Hanoi, Vietnam. E-mail: trinhpv@ims.vast.vn; thangbh@ims.vast.vn; Tel: +84 94 319 0301*

[b]*Graduate University of Science and Technology, Vietnam Academy of Science and Technology, 18 Hoang Quoc Viet Str., Cau Giay Distr., Hanoi, Vietnam*

[c]*VNU University of Engineering and Technology, 144 Xuan Thuy Str., Cau Giay Distr., Hanoi, Vietnam*

mechanical properties and toughening mechanisms of GNPs/epoxy was also reported by H. Chong *et al.* in 2016.[39] To our best knowledge, up to now, there are no experimental studies on the investigation of the effect of the size of GNPs on the properties of the metal composite coatings as well as Ni composite coatings. Thus, this work has been done to investigate the influence of GNPs sizes on the microstructure, microhardness and content of Ni composite coatings. GNPs with different sizes was prepared by high energy ball milling technique for different milling times. The prepared GNPs were functionalized with carboxyl (–COOH) functional groups then dispersed into Watts solutions and co-deposited with ion Ni^{2+} onto the cathode surface *via* electrodeposition technique to form Ni/GNPs nanocomposite coatings. The morphologies, structure and properties of GNPs and Ni/GNPs composite coatings were characterized and presented.

2. Method

2.1. Starting materials

Commercial GNPs (>99% purity) with a thickness of 10–15 nm, the length of 5–7 μm, the true density of 2, 3 g cm^{-3}, and the specific surface area of 3×10^5 cm^2 g^{-1} are purchased from ACS Materials, USA. C1220 copper (Cu > 99,90%) is used as a cathode for the electrodeposition process. Other chemicals purchased from Merck & Co., Inc. are used without any further purification.

2.2. Preparation of GNPs/Ni nanocomposite coatings

The electrodeposition process of GNPs reinforced nickel coating with the different GNPs size is illustrated in Fig. 1. Firstly, as-received GNPs are milled by a high energy ball milling system (8000D Mixer/Mill® – Dual High-Energy Ball Mill, Spex Sample Prep, US) with two symmetry clamps for producing GNPs with different sizes. High energy ball milling uses the back-and-forth shaking motion which is combined with lateral movements of the ends of the vial so that the vial appears to be describing a Fig. 8 or infinity sign as it moves. The dimension of the 8004 tungsten carbide vial set was 5.72 cm height x 6.35 cm diameter, grinding load from 3 cm^3 to 10 cm^3 with two tungsten carbide balls. GNPs are milled with a motor speed of 1425 rpm, clamp movement of 5.9 cm back-and-forth, 2.5 cm side-to-side, clamp speed of 875 cycles per minute for different times of 1 h, 2 h, 3 h, 4 h, and 5 h in argon atmosphere without any chemicals to obtain the different GNP sizes. Secondly, the prepared GNPs are functionalized with carboxyl (–COOH) functional groups by oxidation agents of HNO_3 and H_2SO_4 mixture with 1/3 (v/v) at 70 °C for 5 hours. After the functionalization process, the obtained solutions were centrifuged and washed by distilled water for many times to remove residual chemicals. Afterward, the functionalized GNPs with different sizes are dispersed in 1 lit Watts solutions containing 300 g $NiSO_4 \cdot 6H_2O$, 50 g $NiCl_2 \cdot 6H_2O$, 40 g H_3BO_3 and 0.1 g sodium dodecyl sulfate (SDS) (Table 1). SDS surfactant is added to enhance the wetting for electrodes and the dispersed ability of GNPs.[29,40] As-received mixtures are ultrasonicated for 60 minutes at a temperature of 45 °C to obtain the uniform solutions for electrodeposition processes. Finally, the electrodeposition processes are carried out *via* the three-electrodes electrodeposition system including 2 anodes and 1 cathode. Nickel plate with a size of 40 × 50 × 5 mm is used as the anodes, the copper substrate with the size of 40 × 50 × 1 mm was set as the cathode. Before the electrodeposition process, the copper substrates are grounded by sandpaper with many grit sizes ranged from 240# to 2000# and then polished down by diamond suspension. The polished copper substrates are ultrasonicate with step by step in acetone solution, isopropanol solution, and distilled water for 30 minutes to remove the residual organic components. Electrodeposition processes were carried out for 90 minutes with the experimental conditions as presented in Table 1. The pristine Ni coating deposited from Watts solutions without GNPs components was prepared at the same conditions to compare.

2.3. Characterization techniques

Milled GNPs and Ni/GNPs coating are investigated with the types of equipment as the following: Raman Spectroscopy (LabRAM HR 800, HORIBA Jobin Yvon – France) with a 532 nm laser as an excitation source is used to study GNPs structure. The microstructure of GNPs and the coatings are investigated by FESEM (Hitachi S4800, Japan), GNPs thickness is evaluated by atomic force microscopy (AFM) (XE-100 Park Systems). The

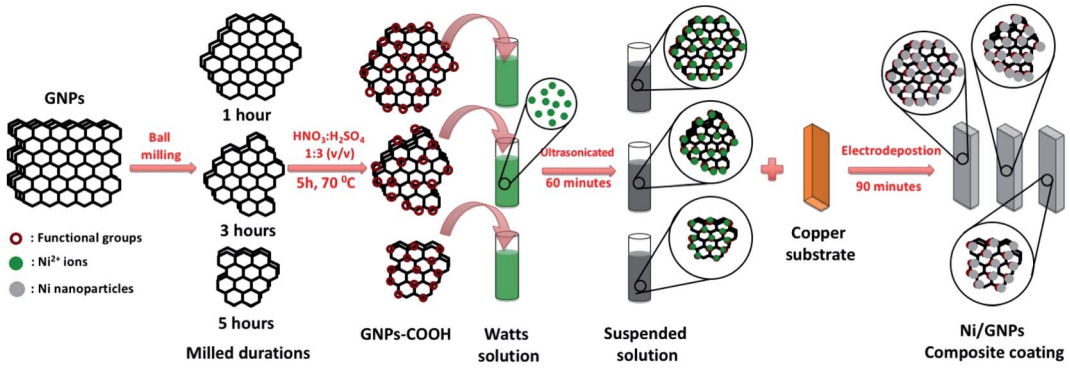

Fig. 1 Illustration of the fabrication process of GNPs reinforced nickel coating with the different GNPs size using the electrodeposition technique.

Table 1 Plating conditions

	Functionalized GNPs material								
Coating sample	GNPs sample	Milled duration	Concentration	Watts solution	Current density	Temp.	pH	Stirring speed	Plating time
Ni	—	—	—	1 l	2.5 A dm^{-2}	45 °C	4–5	100 rpm	90 min
Ni-GNPs1	GNPs1	1 h	0.3 g l^{-1}						
Ni-GNPs2	GNPs2	2 h							
Ni-GNPs3	GNPs3	3 h							
Ni-GNPs4	GNPs4	4 h							
Ni-GNPs5	GNPs5	5 h							

composition of the coatings is analyzed using SEM energy dispersive spectroscopy (SEM-EDS) (S-4800; Hitachi, Japan). The thickness of the coatings is estimated with a model Axiovert 40MAT from Carl Zeiss, Germany. The microhardness of the coatings is measured by using a microhardness tester (model Indenta Met 1106) from Buehler, USA. BET measurement is carried out on Autosorb-iQ-MP (02142-1) system (USA). Zeta-size analyzation is measured by a Malvern ZS Nano S analyzer. FTIR analysis is performed by a SHIMADZU IR Prestige21 Spectrometer. The XRD patterns of the coatings are recorded by using an ARL EQUINOX 5000 X-ray diffractometer equipped with CuKα radiation. The XRD data are analyzed by the Rietveld method using the GSAS-2 program.

3. Results and discussion

3.1. Characterization of milled GNPs

Fig. 2 shows SEM images of GNPs prepared with different milling times. As can be seen, the pristine GNPs exhibit a diameter in a range from 3 μm to 5 μm, flat surfaces, and agglomerated with each other (Fig. 2a). The size and surface morphology of GNPs are changed significantly after milling. In this process, GNPs are exfoliated and broken into smaller layers. The statistical spectra of GNPs size collected from more than 100 GNPs on SEM images. Fig. 2b–d show that in the case of GNPs1, the sizes ranged from around 250 nm to about 600 nm, they reached a peak of around 20% at the size of 400 nm. For GNPs3, the sizes vary between 200 nm and 450 nm, they reach a peak of 35% at the size of 250 nm. For the last case, GNPs5 sizes fluctuate from around 100 nm to about 300 nm, they reach a peak of around 40% at the size of 200 nm. The obtained results imply that GNPs sizes changed with the change of the milling times, the longer milling time is applied, the smaller GNPs size is. In addition, few fractures marks are observed on the surface and boundary of the milled GNPs. This demonstrated that the ball milling process affected the GNPs structure.

The thickness of GNPs treated with the different milling times is evaluated by AFM as shown in Fig. 3. The thickness of the initial GNPs is measured to be around 12 nm (Fig. 3a). Fig. 3e shows the thickness statistics of milled GNPs which are

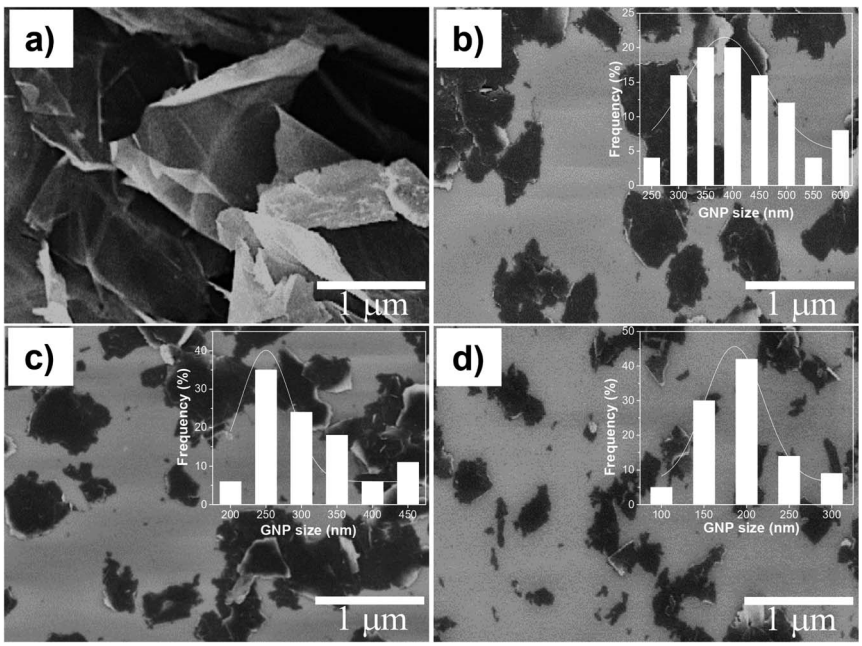

Fig. 2 FESEM images of (a) pristine GNPs and GNPs milled with different times of (b) 1 h, (c) 3 h and (d) 5 h.

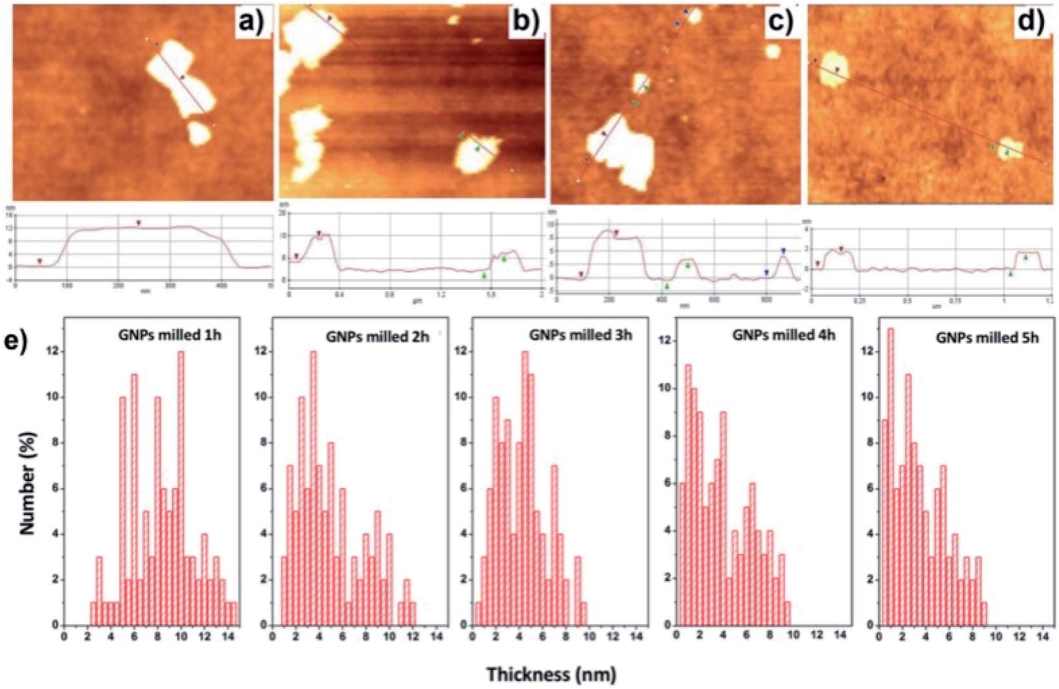

Fig. 3 The typical AFM images of (a) GNPs (b) GNPs1, (c) GNPs3, (d) GNPs5 and (e) the thickness distributions of GNPs with different milling times.

collected from 100 plates GNPs on the SiO_2 substrates for each sample. As can be seen, the thickness of GNPs1 fluctuates from around 5 nm to about 12 nm. In the case of increasing the milling time, the thickness spectrum peaks move to the left direction, which implies the decrease of GNPs thickness. In the GNPs3 case, the thickness is distributed in a range from 2 nm to 6 nm and reached a peak of around 4.5 nm which occupy about 12%. For GNPs5, the thickness ranges from around 0.5 nm to about 4 nm and reaches a peak of 1 nm which occupies over 12%. The obtained results indicate that the GNPs thickness is decreased with the increase of the milling times.

Raman spectra analysis is carried out to evaluate the influence of the ball milling process on GNPs structure. Fig. 4 shows the Raman spectra of GNPs with different milling times, where

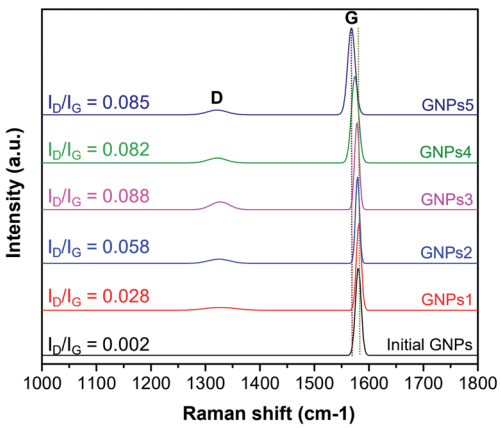

Fig. 4 Raman spectra of GNPs with different milling times.

emerged the typical peaks of GNPs including G peak at 1580 cm^{-1} assigned to the graphite structure, and D peak at the range of 1340 cm^{-1} assigned to the defects in GNPs structure and the presence of impurity or amorphous carbon.[41–43] The measured results indicated that the structure of GNPs is slightly changed with different milling times. There is almost no D peak in the initial GNPs which implies the high quality and purity of the as-received GNPs. For the milled GNPs, Raman spectra emerge D peaks in which the intensities increase with the milling times. The I_D/I_G intensity ratios were calculated to be 0.028, 0.058, 0.088, 0.082 and 0.085 corresponding to GNPs1, GNPs2, GNPs3, GNPs4 and GNPs5, respectively. However, the increase of the I_D/I_G ratio of the milled GNPs is quite small compared to that of initial GNPs. This means the defects in the structure of GNPs are inconsequential. It is interesting to note that, the G peak of the milled GNPs is slightly moved to lower wavenumber. This could be due to the compressive strain induced in the ball milling process caused a shift in the G-band position.[44–46] X-ray diffraction was also employed to characterize the structural changes of GNPs during the ball milling process. Fig. 5 exhibits that compared to the diffraction peak of pristine GNPs, the interlayer diffraction (002) peak of the milled GNPs is broadened and the (004) peak gradually disappeared while the intensity of (002) declines with the milling time, these are attributed to the decrease of GNPs layer thickness.[47,48]

GNPs were functionalized the –COOH functional groups to enhance the dispersed ability into the plating solution. Fig. 6 shows the FTIR spectra of milled GNPs functionalized with COOH functional groups. The absorption peaks around 3400 cm^{-1}, 1720 cm^{-1}, 1365 cm^{-1} and 1080 cm^{-1} of wavenumber are assigned to the presence of the –OH groups of residual water, the

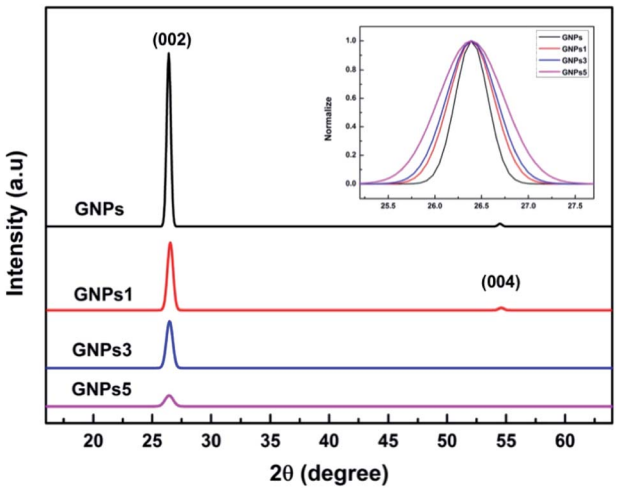

Fig. 5 XRD patterns of pristine GNPs and milled GNPs.

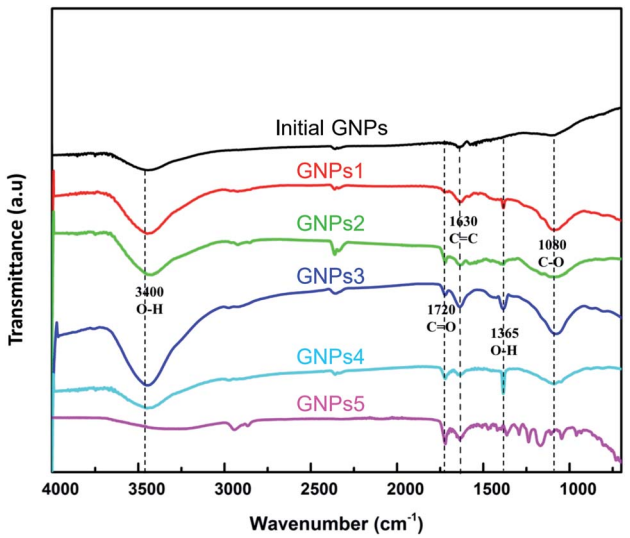

Fig. 6 FTIR spectra of functionalized GNPs with different milling times.

C=O bonding in –COOH groups, the –OH bonding and the C–O stretching vibrations mode in the –COOH groups, respectively. Besides, the peaks at 1630 cm^{-1} are assigned to the C=C bonding of carbon atoms in the graphite structure.[49–52] In the case of pristine GNPs, there is no presence of functional groups formed between oxygen, hydrogen and carbon element besides the C=C bonding of carbon atoms. These results reveal that the –COOH functional groups are formed on the surface of GNPs after the functionalization process.

The functionalized GNPs with different sizes (GNPs1, GNPs2, GNPs3, GNPs4, GNPs5) are dispersed into distilled water in order to evaluate the dispersed ability and stability. Fig. 7a shows the size distribution of GNPs with different milling times. The peaks of the GNPs size spectra shift steadily to the small size direction, and the FWHMs narrow gradually as increasing the milling times. GNPs sizes reach a saturated size after milling time of 5 hours, its sizes were unable to reduce any more. However, FWHM narrows slightly, the peak of GNPs5 size spectrum stays at around 120 nm occupy about 15% while GNPs5 sizes over 500 nm fall dramatically occupied 2.5% amount of GNPs5. In addition, the size distribution of GNPs1, GNPs2, GNPs3, GNPs4, GNPs5 has only one peak that indicates the good dispersion of the functionalized GNPs in distilled water without any agglomerations. Besides, the measured zeta potential values of GNPs increase gradually from 17 mV to 29 mV corresponding to GNPs1 and GNPs5 (Fig. 7b). This means the milled GNPs have a pretty stable state in water.[53–56] This is attributed to the decrease of GNPs sizes leading to the increase of surface area and the increase of the –COOH functional groups attached to the surface and boundary of GNPs. The obtained results demonstrate that the high energy ball milling method is an effective method to reduce the GNPs size, exfoliate GNPs into the thinner plates, increasing the surface area, the dispersion ability, and stability of GNPs in distilled water.

3.2. Characterization of Ni/GNPs nanocomposite coatings

Fig. 8 is the characteristic microstructure images of Ni, Ni/GNPs1, Ni/GNPs2, Ni/GNPs3, Ni/GNPs4, Ni/GNPs5 coatings. For pristine Ni coating, the grain sizes are the largest, which ranges from 2 μm to 5 μm (Fig. 8a). When the coatings are reinforced by GNPs materials including GNPs1, GNPs2, GNPs3, GNPs4, GNPs5, the grain size of the composite coatings reduce with the decrease of GNPs sizes, which is from around several micrometers to about several hundred nanometers (Fig. 8b–f). As a result, the smallest grain size is observed on the coating reinforced by GNPs5. This result demonstrates that the sizes of GNPs influence dramatically on the formation and growth of nickel crystallite. The smaller GNPs sizes are, the smaller the nickel grain sizes are. Besides, SEM images show the different mechanisms in forming the nickel crystallite concerning the different GNPs sizes. For the large GNPs sizes (GNPs1, GNPs3), nickel crystal nucleations are formed and grew in the GNPs surface (inserted in Fig. 8b and d). However, in the case of GNPs5 (inserted in Fig. 8f), the smaller GNPs sizes intercalated inside the formed crystal nucleations lead to the prevention of the oriented crystal growth, this caused the decrease of nickel grain size.

Fig. 9 shows the cross-section images of the coatings. The presented results are obtained from the average value of ten points along with the cross-section image at the same position on patterns. The thickness was measured to be 33.42 μm, 30.05 μm, 31.33 μm, 32.01 μm, 32.92 μm, 33.24 μm corresponding to Ni, Ni/GNPs1, Ni/GNPs2, Ni/GNPs3, Ni/GNPs4, Ni/GNPs5 nanocomposite coating, respectively. The thickness of the GNPs reinforced Ni coatings are thinner than that of the pristine Ni coating. This result demonstrates that the presence of GNPs has declined slightly the current efficiency. In addition, as can be seen in cross-section images, the thickness of the coating depends on GNPs sizes, the smaller the GNPs sizes are, the thicker the coatings are. This indicates that the small GNPs sizes can increase the current efficiency in Watt solutions.

In order to evaluate the carbon content of the coatings, the EDS analysis is carried out. As shown in Fig. 10, there is not any carbon component inside the Ni coating, the nickel content

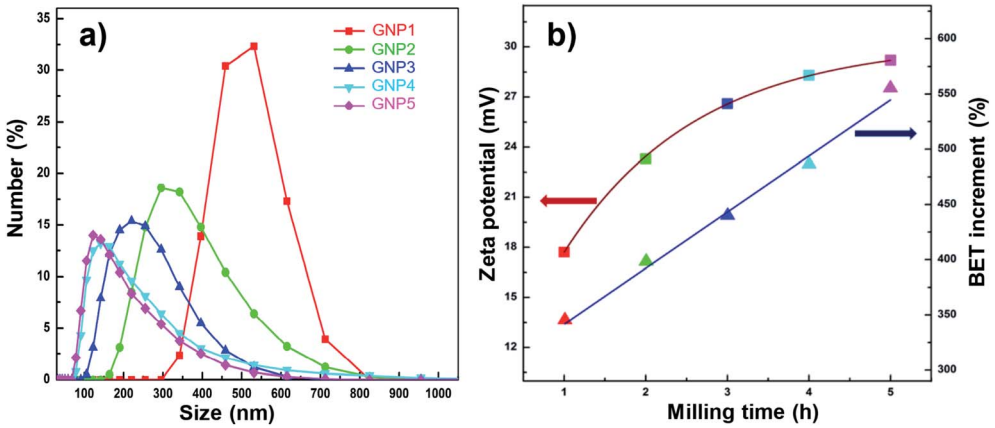

Fig. 7 (a) Size distribution and (b) Zeta potential and BET surface area of GNPs with different milling times.

occupies 100 wt%. For the GNPs reinforced Ni coatings, the carbon contents occupy from around 6.77 wt% to about 16.41 wt% of coatings. Although all of the Watts solutions have the same GNPs concentration, the carbon contents in coatings vary with each the GNPs sizes. The smaller the GNPs sizes are, the higher the carbon content in the coatings are. This is attributed to the high surface area of the small GNPs sizes leading to the high absorption ability in the co-deposited process of nickel ion and GNPs materials.

Fig. 11 shows the XRD patterns of Ni coating and GNPs reinforced Ni coatings. All patterns show the typical peaks of nickel components which grow along the (111), (200) and (220).

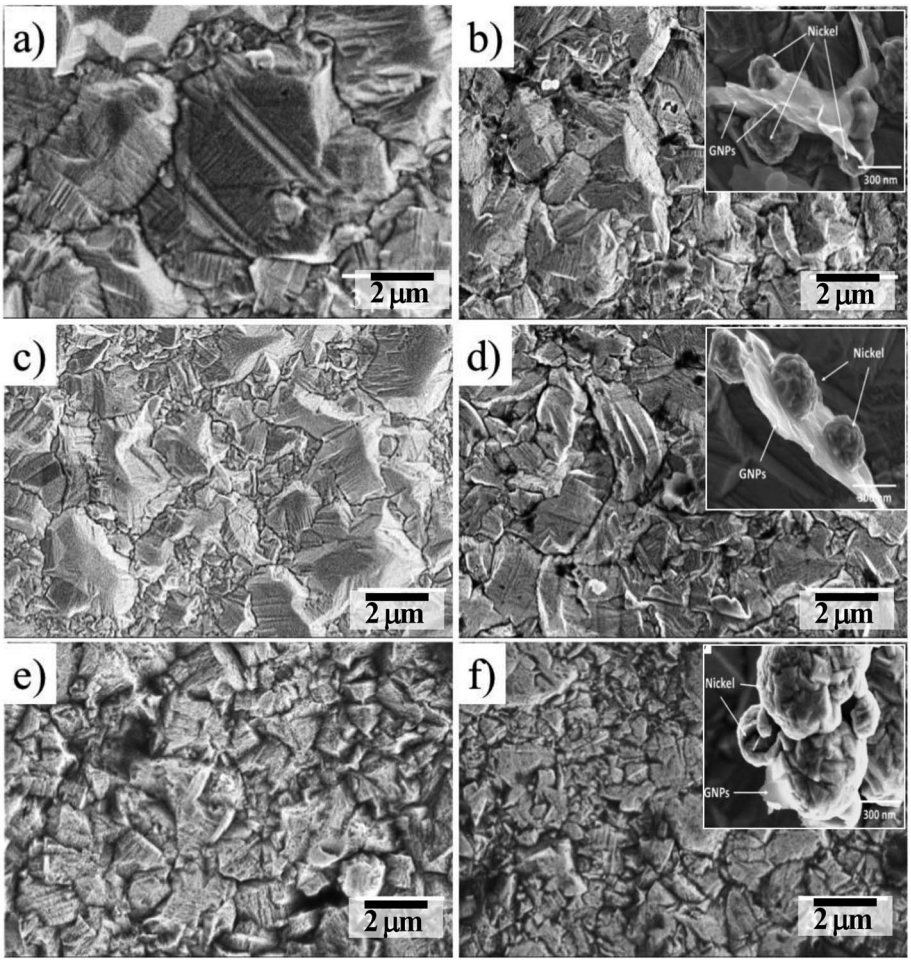

Fig. 8 FESEM images of the surface coatings (a) Ni, (b) Ni/GNPs1, (c) Ni/GNPs2, (d) Ni/GNPs3, (e) Ni/GNPs4, (f) Ni/GNPs5.

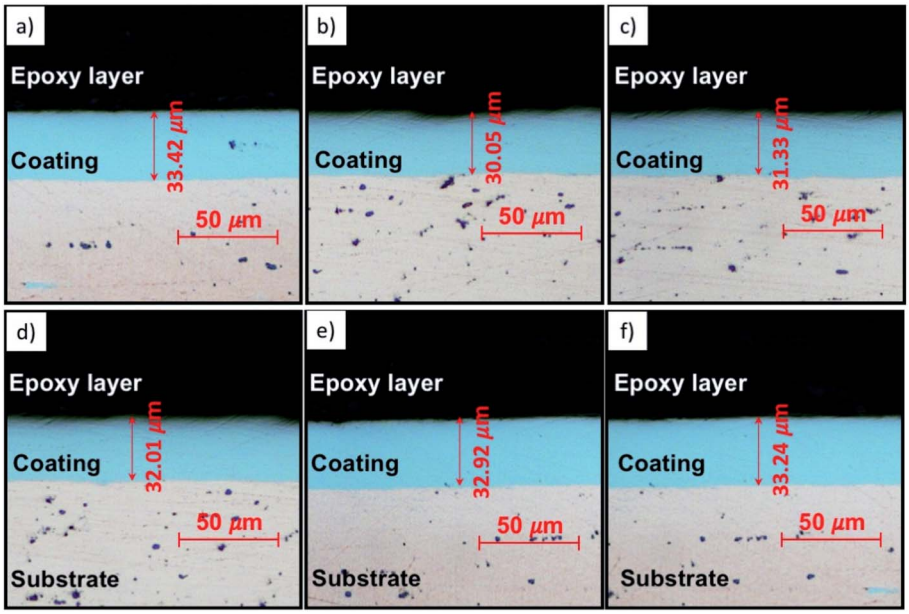

Fig. 9 Cross-sectional optical images of (a) Ni, (b) Ni/GNPs1, (c) Ni/GNPs2, (d) Ni/GNPs3, (e) Ni/GNPs4, (f) Ni/GNPs5.

It is noted that there is a slight change of preferred orientation nickel growth in coatings. For pristine Ni coating, the preferred orientation grows along (111) with the highest intensity, the next preferred orientation grows along (200) and the preferred orientation grows along (220) with the lowest intensity. In the case of the GNPs reinforced Ni coating, there is a steady decrease in the intensity of the preferred orientation growing along (200), which compared to the preferred orientation growing along (220). This demonstrates that the smaller the GNPs sizes are, the more significantly the preferred orientation growing along (200) decreases.

Basing on the XRD patterns of coatings and incorporating to Debye–Scherrer equation $L = \left(\frac{K\lambda}{\beta \cos \theta}\right)$ in which: L is the average crystalline size, K is the Scherrer constant, λ is the wavelength, β is Full width at half maximum and θ is the diffraction angle,[23,29] the average nickel crystallite size of the coatings is calculated. The change of the average nickel

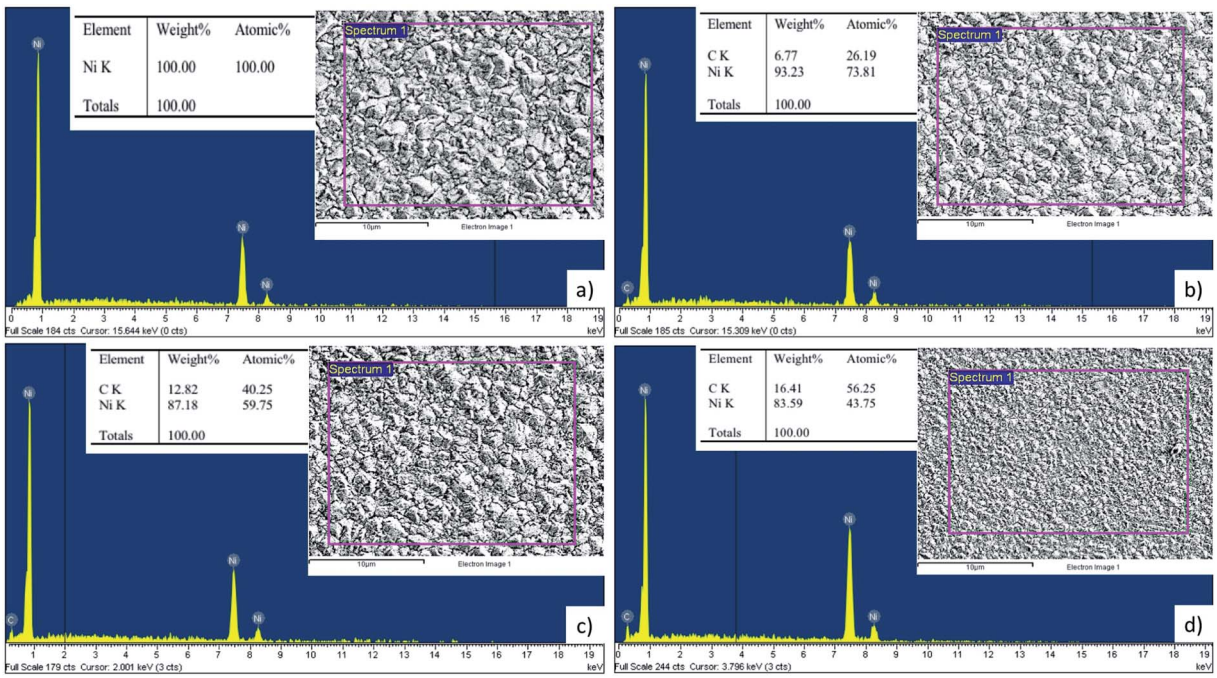

Fig. 10 EDS results of some selected coatings (a) Ni, (b) Ni/GNPs1, (c) Ni/GNPs3, (d) Ni/GNPs5.

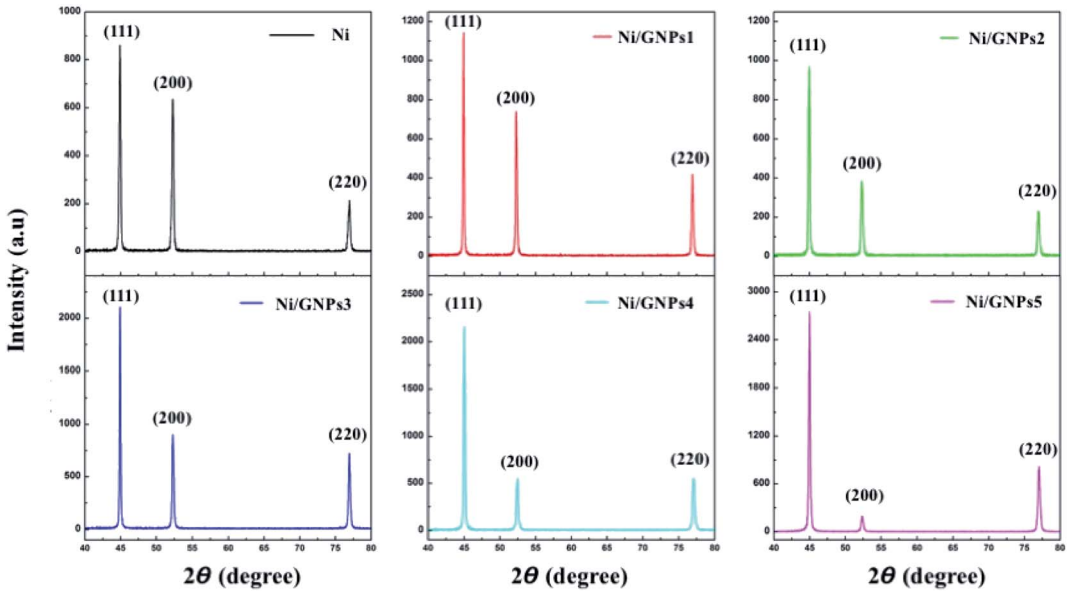

Fig. 11 XRD patterns of Ni-GNP nanocomposite coatings.

crystallite size with the GNPs sizes as shown in Fig. 12. For the pure Ni coating, the average crystallite size is around 25.61 nm. As containing GNPs content, the average crystallite size decreases significantly to about 18.35 nm for Ni/GNPs1 coating. In the case of Ni/GNPs2, Ni/GNPs3, Ni/GNPs4, and Ni/GNPs5, the average crystallite size declines gradually to around 17.23 nm, 15.35 nm, 13.49 nm, and 12.74 nm, respectively. The obtained results again confirmed the influence of the GNPs sizes on the nickel crystal growth.

Microhardness of Ni and the Ni/GNPs nanocomposite coatings are shown in Fig. 12. The obtained results are the average of 20 measured points in a composite coating sample. For the pristine Ni coating, the hardness is 186 HV. For Ni/GNPs nanocomposite coatings, the microhardness is measured to be 229 HV, 238 HV, 256 HV, 268 HV, 273 HV corresponding to Ni/GNPs1, Ni/GNPs2, Ni/GNPs3, Ni/GNPs4, Ni/GNPs5 nanocomposite coatings, respectively. As a result, the nanocomposite coatings containing 5 h-milled GNPs have the highest microhardness, which is increased up to 47% compared to pristine Ni coating. Table 2 presents the reported microhardness of nickel–graphene nanocomposite coatings. Comparing to other reports, the obtained results are in line with the earlier report by Dong *et al.*,[58] in which using graphene as an additive component for the nanocomposite. Some other studies reported very high hardness coatings.[23,24,29,34,35] But it is noted that they used GO as a reinforcement component, higher GO concentration and/or higher surfactant concentration. For example, Yasin *et al.*[35] reported a very high microhardness (503 HV) for the nanocomposite coating as using GO as a reinforcement component with a concentration up to 0.4 g l^{-1}. The influence of Gr and surfactant concentration on the microhardness of the coating has not been focused on our current study. This will be done in future work to find the best conditions for preparing the nanocomposite coating with the highest performance. The enhancement in microhardness of the coating is attributed to the uniform dispersion of the small GNPs sizes in Watts solution lead to the uniform distribution of this material inside the nickel matrix. The presence of GNPs components inside the nickel matrix results in the enhancement of microhardness of nickel coatings, this is demonstrated in previous studies[23,28,56,57,59] through the strengthening mechanisms such as thermal expansion coefficient mismatch, Orowan looping, load transfer.[60] In addition, the small GNPs size decreases the Ni grain size causing the formation of the grain refinement effect as demonstrated in previous sections. The relationship between the hardness and grain size are demonstrated through the Hall–Petch equation: $H_V = H_0 + k_H d^{-1/2}$, where H_0 and k_H are constants, d is the grain size.[61] This relationship indicates that the microhardness depends

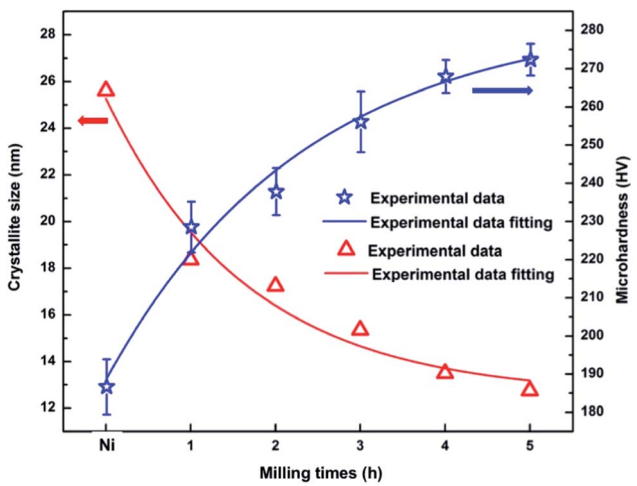

Fig. 12 Microhardness and crystallite size of electrodeposited coatings Ni and Ni/GNPs1, Ni/GNPs2, Ni/GNPs3, Ni/GNPs4, Ni/GNPs5 corresponding to the milled graphene 1 hour, 2 hours, 3 hours, 4 hours and 5 hours.

Table 2 A literature review on microhardness of nickel–graphene nanocomposite coatings

No.	Plating method	Reinforced material	Microhardness of coating			Ref.
			Pristine Ni	Ni/Graphene	% Enhancing	
1	Direct current, current density 9 A dm^{-2}, SDS 0.4 g l^{-1},	rGO (0.2g l^{-1})	—	~500 HV	—	34
2	Direct current, current density 5 A dm^{-2}, SDS 0.4 g l^{-1}	rGO (0.2g l^{-1})	—	~500 HV	—	40
3	Direct current, SDS 0.4 g l^{-1}	rGO (0.4 g l^{-1})	235 HV	503 HV	114%	35
4	Pulse current, current density 5 A dm^{-2}, SDS 0.2 g l^{-1}, temperature 45 °C	rGO (0.5 g l^{-1})	—	492 HV	—	24
5	Direct current, current density 5 A dm^{-2}, SDS 0.4 g l^{-1}, temperature 45 °C	rGO (0.2 g l^{-1})	—	500 HV	—	29
6	Current density 1 A dm^{-2}, SDS 0.2 g l^{-1}, temperature 40 °C	rGO (0.1 g l^{-1})	287 HV	385 HV	~34%	23
7	Direct current, current density 5 A dm^{-2}, temperature 55 °C	GO (1 g l^{-1})	1.81 GPa	6.85 GPa	278%	28
8	Direct current, current density 0.15 A dm^{-2}, SDS 0.5 g l^{-1}, temperature 50 °C	rGO (0.05 g l^{-1})	3.83 GPa	4.6 GPa	~20%	27
9	Pulse current, current density 1 A dm^{-2}, SDBS 0.05 g l^{-1},	rGO (0.4 g l^{-1})	—	223 HV	—	58
10	One-step electrodeposited Ni/graphene composite	Exfoliated graphite	265 HV	427 HV	~61%	60
11	Electrophoretic-deposition	Gr powder	—	181.78 HV	—	61
12	Direct current, current density 2.5 A dm^{-2}, SDS 0.1 g l^{-1}, temperature 45 °C	GNPs (0.3 g l^{-1})	186 HV	273 HV	~47%	This work

considerably on the grain size, the smaller the grain sizes are, the harder the coating is. This result demonstrates that the small GNPs size plays an important role in the strengthening mechanisms for nickel coating.

From experimental data of crystallite size and microhardness we can derive the relationship between crystallite size and microhardness as a function of milling times by experimental data fitting as the following equations:

$$d = K_z e^{(-t/1.67)} + d_\alpha \quad (1)$$

$$H_c = K_H e^{(-t/2.34)} + H_\alpha \quad (2)$$

Eqn (1) describes the dependence of the crystallite size of Ni matrix on the milling time of GNPs in which $d_\alpha = 12.54$ is a constant with a dimension [nm], $K_z = 12.74$ is a scale factor depending on properties of the reinforced material. Eqn (2) is used for predicting the change of the microhardness of the nanocomposite coating, in which $H_\alpha = 283.76$ is a constant with a dimension [HV], $K_H = -94.95$ is a scale factor depending on properties of the reinforced material. Based on eqn (1) and (2) we can predict the saturated value of crystallite size around 12.54 nm and microhardness about 283.76 HV when milling time is increased to infinity. These are also reasons why we have limited milling time for 5 hours.

4. Conclusions

We have investigated the effect of graphene nanoplatelet size on the microstructure and hardness of the electrodeposited nickel/graphene nanocomposite coatings. The graphene nanoplatelet (GNPs) size is modified by using a high energy ball milling technique. The milled GNPs are functionalized with carboxylic functional groups to prepare for nickel electrodeposition processes. The dispersion ability of the milled GNPs can be significantly improved with the increase in the milling time. The best milling time condition for GNPs is determined of 5 hours, in which milled GNPs have a size of 180 nm, good dispersion ability, and high surface area. Besides, the obtained results demonstrate that the reinforced ability of the small GNPs size is better, the microhardness of the GNPs5 reinforced nickel increased to around 47% compared to the pristine Ni coating with the carbon content occupied of 16.41 wt%.

Conflicts of interest

There are no conflicts to declare.

Acknowledgements

The research was financially supported by Vietnam Academy of Science and Technology under project coded QTBY01.02/19-20.

References

1 A. Torrents, H. Yang and F. A. Mohamed, *Metall. Mater. Trans. A*, 2010, **41**, 621–630.
2 H. W. Höppel and M. Göken, *Nanostructured Metals and Alloys*, 2011.
3 S. Suresh, A. Mortensen and A. Needleman, *Fundamentals of metal-matrix composites*, 1993.
4 J. Reid, *Jpn. J. Appl. Phys.*, 2001, **40**, 2650–2657.

5 C. Lupi and D. Pilone, *Miner. Eng.*, 2001, **14**, 1403–1410.
6 S. Rashmi, L. Elias and A. Chitharanjan Hegde, *Eng. Sci. Technol. Int. J.*, 2017, **20**, 1227–1232.
7 M. R. H. de Almeida, E. P. Barbano, M. F. de Carvalho, P. C. Tulio and I. A. Carlos, *Appl. Surf. Sci.*, 2015, **333**, 13–22.
8 J. Musil, *Surf. Coat. Technol.*, 2000, **125**, 322–330.
9 P. Holubar, M. Jilek and M. Sima, *Surf. Coat. Technol.*, 2000, **133–134**, 145–151.
10 R. Andrievski, *Mater. Trans.*, 2001, **42**, 1471–1473.
11 K. S. Novoselov, A. K. Geim, S. V. Morozov, D. Jiang, M. I. Katsnelson, I. V. Grigorieva, S. V. Dubonos and A. A. Firsov, *Nature*, 2005, **438**, 197–200.
12 C. Lee, X. Wei, J. W. Kysar and J. Hone, *Science*, 2008, **321**, 385–388.
13 D. G. Papageorgiou, I. A. Kinloch and R. J. Young, *Prog. Mater. Sci.*, 2017, **90**, 75–127.
14 J. F. Dai, G. J. Wang, L. Ma and C. K. Wu, *Rev. Adv. Mater. Sci.*, 2015, **40**, 60–71.
15 P. Govindaraj, B. Fox, P. Aitchison and N. Hameed, *Ind. Eng. Chem. Res.*, 2019, **58**, 17106–17129.
16 H. Porwal, S. Grasso and M. J. Reece, *Adv. Appl. Ceram.*, 2013, **112**, 443–454.
17 Z. Hu, G. Tong, D. Lin, C. Chen, H. Guo, J. Xu and L. Zhou, *Mater. Sci. Technol.*, 2016, **32**, 930–953.
18 J. R. Potts, D. R. Dreyer, C. W. Bielawski and R. S. Ruoff, *Polymer*, 2011, **52**, 5–25.
19 H. Chang and H. Wu, *Energy Environ. Sci.*, 2013, **6**, 3483–3507.
20 G. Yasin, M. Arif, T. Mehtab, M. Shakeel, M. A. Mushtaq, A. Kumar, T. A. Nguyen, Y. Slimani, M. T. Nazir and H. Song, *Inorg. Chem. Front.*, 2020, **7**, 402–410.
21 S. Ullah, G. Yasin, A. Ahmad, L. Qin, Q. Yuan, A. U. Khan, U. A. Khan, A. U. Rahman and Y. Slimani, *Inorg. Chem. Front.*, 2020, **7**, 1750–1761.
22 H. G. P. Kumar and M. A. Xavior, *Procedia Eng.*, 2014, **97**, 1033–1040.
23 C. M. P. Kumar, T. V Venkatesha and R. Shabadi, *Mater. Res. Bull.*, 2013, **48**, 1477–1483.
24 H. Algul, M. Tokur, S. Ozcan, M. Uysal, T. Cetinkaya, H. Akbulut and A. Alp, *Appl. Surf. Sci.*, 2015, **359**, 340–348.
25 B. Szeptycka, A. Gajewska-midzialek and T. Babul, *J. Mater. Eng. Perform.*, 2016, **25**, 3134–3138.
26 Y. Liu, Y. Liu, Q. Zhang, C. Zhang, J. Wang, Y. Wu, P. Han, Z. Gao, L. Wang and X. Wu, *Mater. Sci. Eng. A*, 2018, **727**, 133–139.
27 Z. Ren, N. Meng, K. Shehzad, Y. Xu, S. Qu, B. Yu and J. K. Luo, *Nanotechnology*, 2015, **26**, 065706.
28 D. Kuang, L. Xu, L. Liu, W. Hu and Y. Wu, *Appl. Surf. Sci.*, 2013, **273**, 484–490.
29 A. Jabbar, G. Yasin, W. Q. Khan, M. Y. Anwar, R. M. Korai, M. N. Nizam and G. Muhyodin, *RSC Adv.*, 2017, **7**, 31100–31109.
30 J. Li, Z. An, Z. Wang, M. Toda and T. Ono, *ACS Appl. Mater. Interfaces*, 2016, **8**, 3969–3976.
31 S. Singh, S. Samanta, A. K. Das and R. R. Sahoo, *Surfaces and Interfaces*, 2018, **12**, 61–70.
32 Y. Liu, Y. Liu, Q. Zhang, C. Zhang, J. Wang, Y. Wu, P. Han, Z. Gao, L. Wang and X. Wu, *Mater. Sci. Eng. A*, 2018, **727**, 133–139.
33 G. Yasin, M. Arif, M. N. Nizam, M. Shakeel, M. A. Khan, W. Q. Khan, T. M. Hassan, Z. Abbas, I. Farahbakhsh and Y. Zuo, *RSC Adv.*, 2018, **8**, 20039–20047.
34 G. Yasin, M. Arif, M. Shakeel, Y. Dun, Y. Zuo, W. Q. Khan, Y. Tang, A. Khan and M. Nadeem, *Adv. Eng. Mater.*, 2018, **20**, 1701166.
35 G. Yasin, M. A. Khan, M. Arif, M. Shakeel, T. M. Hassan, W. Q. Khan, R. M. Korai, Z. Abbas and Y. Zuo, *J. Alloys Compd.*, 2018, **755**, 79–88.
36 G. Yasin, M. J. Anjum, M. U. Malik, M. A. Khan, W. Q. Khan, M. Arif, T. Mehtab, T. A. Nguyen, Y. Slimani, M. Tabish, D. Ali and Y. Zuo, *Diam. Relat. Mater.*, 2020, **104**, 107763.
37 G. Dai and L. Mishnaevsky, *Comput. Mater. Sci.*, 2014, **95**, 684–692.
38 F. Wang, L. T. Drzal, Y. Qin and Z. Huang, *J. Mater. Sci.*, 2015, **50**, 1082–1093.
39 H. M. Chong, S. J. Hinder and A. C. Taylor, *J. Mater. Sci.*, 2016, **51**, 8764–8790.
40 G. Yasin, M. Arif, M. N. Nizam, M. Shakeel, M. A. Khan, W. Q. Khan, T. M. Hassan, Z. Abbas, I. Farahbakhsh and Y. Zuo, *RSC Adv.*, 2018, **8**, 20039–20047.
41 A. Reina, X. Jia, J. Ho, D. Nezich, H. Son, V. Bulovic, M. S. Dresselhaus and J. Kong, *Nano Lett.*, 2009, **9**, 30–35.
42 V. T. Nguyen, H. D. Le, V. C. Nguyen, T. T. T. Ngo, D. Q. Le, X. N. Nguyen and N. M. Phan, *Adv. Nat. Sci. Nanosci. Nanotechnol.*, 2013, **4**(3), 035012.
43 X. Dong, P. Wang, W. Fang, C. Y. Su, Y. H. Chen, L. J. Li, W. Huang and P. Chen, *Carbon*, 2011, **49**, 3672–3678.
44 Z. H. Ni, T. Yu, Y. H. Lu, Y. Y. Wang, Y. P. Feng and Z. X. Shen, *ACS Nano*, 2008, **2**, 2301–2305.
45 V. N. Popov and P. Lambin, *Phys. Rev. B*, 2013, **87**, 155425.
46 M. Huang, H. Yan, T. F. Heinz and J. Hone, *Nano Lett.*, 2010, **10**, 4074–4079.
47 L. Liu, Z. Xiong, D. Hu, G. Wu and P. Chen, *Chem. Commun.*, 2013, **49**, 7890.
48 Y. Lv, L. Yu, C. Jiang, S. Chen and Z. Nie, *RSC Adv.*, 2014, **4**, 13350.
49 J. Zhang, H. Zou, Q. Qing, Y. Yang, Q. Li, Z. Liu, X. Guo and Z. Du, *J. Phys. Chem. B*, 2003, **107**, 3712–3718.
50 J. Jang, J. Bae and S. H. Yoon, *J. Mater. Chem.*, 2003, **13**, 676–681.
51 B. H. Thang, P. Van Trinh, L. D. Quang, N. T. Huong, P. H. Khoi and P. N. Minh, *J. Korean Phys. Soc.*, 2014, **65**, 312–316.
52 P. Van Trinh, N. N. Anh, N. T. Tam, N. T. Hong, P. N. Hong, P. N. Minh and B. H. Thang, *RSC Adv.*, 2017, **7**, 49937–49946.
53 P. Van Trinh, N. N. Anh, N. T. Hong, P. N. Hong, P. N. Minh and B. H. Thang, *J. Mol. Liq.*, 2018, **269**, 344–353.
54 A. Ghadimi, R. Saidur and H. S. C. Metselaar, *Int. J. Heat Mass Tran.*, 2011, **54**, 4051–4068.
55 J. Ivall, G. Langlois-Rahme, S. Coulombe and P. Servio, *Nanotechnology*, 2017, **28**, 055702.

56 T. Van Hau, P. Van Trinh, N. P. Hoai Nam, V. D. Lam, P. N. Minh and B. H. Thang, *Mater. Res. Express*, 2019, **6**, 0850c4.
57 L. Xiang, Q. Shen, Y. Zhang, W. Bai and C. Nie, *Surf. Coat. Technol.*, 2019, **373**, 38–46.
58 Y. Dong, W. Sun, X. Liu, M. Ma, Y. Zhang and Y. Liu, *Adv. Eng. Mater.*, 2019, **21**, 1900327.
59 A. Saboori, M. Dadkhah, P. Fino and M. Pavese, *Metals*, 2018, **8**, 423.
60 X. D. Liu, M. Nagumo and M. Umemoto, *Mater. Trans. JIM*, 1997, **38**, 1033–1039.
61 J. Chen, J. Li, D. Xiong, Y. He, Y. Ji and Y. Qin, *Appl. Surf. Sci.*, 2016, **361**, 49–56.

